Proceedings of the Canadian Society for Mechanical Engineering International Congress
Computational Fluid Dynamics Canada International Congress
CSME - CFD-SC2023
May 28-31, 2023, Sherbrooke, QC, Canada

Acoustic far-field prediction of a Controlled Diffusion airfoil self-noise

Andrea Arroyo Ramo[1,2], Stéphane Moreau[1], Michaël Bauerheim[2], Richard D. Sandberg[3]

[1]Faculté de Génie, Université de Sherbrooke Sherbrooke, Canada
[2]Département Aérodynamique, Énergetique et Propulsion, ISAE-Supaero, Toulouse, France
[3]Department of Mechanical Engineering, the University of Melbourne, Melbourne, Australia

***Abstract*—**Direct Numerical Simulations (DNS) of the compressible flow over a Controlled Diffusion (CD) airfoil are conducted. To obtain far field predictions, the DNS are coupled to an acoustic solver based on the Ffowcs Williams & Hawkings formulation. The turbulent flow field at the vicinity of the trailing edge and its noise generation mechanisms is the object of study. The installation effects associated with wind tunnel conditions are included in the computations. Three noise sources have been found, the flow separation and reattachment, the interaction between the attached turbulent flow at the trailing edge and a secondary instability in the near wake.

***Keywords-component*—CFD, DNS, Aeroacoustics, Airfoil noise**

I. Introduction

Noise is a generalized concern in most of the industrial applications. In particular, it features in turbomachinery appliances such as engine cooling fans, wind turbines or high-speed turboengines. Among all the noise sources in turbomachinery, airfoil noise is an important contributor to the total noise emitted since it is responsible for the minimum noise level produced when the airfoil encounters a homogeneous stationary flow. The blade self-noise is produced by the interaction of turbulent eddies in the turbulent boundary layer (BL) and the wake with the airfoil itself. This noise of broadband nature can become the dominant noise source in the absence of other interaction sources. In the present study, the broadband noise generated by the interaction of the turbulent airfoil boundary layer flow with the trailing edge is addressed, with the purpose of producing airfoil noise predictions.

Numerical predictions of airfoil self-noise have been recently reviewed in [1]. In the present work, to study trailing-edge noise, the approach based on the acoustic formulation of Ffowcs Williams & Hawkings [2] is employed. This work follows last decade's trends, in which high-fidelity compressible simulations (Large Eddy Simulations –LES– [3], [4], and Direct Numerical Simulations –DNS– [5]–[8]) have been used to perform predictions of trailing-edge noise. The high-fidelity simulations are coupled with an acoustic solver to propagate the acoustics resolved in the near field towards the far field.

The objective of the present work is to investigate the turbulent flow field and the contribution of the different noise sources to the airfoil noise, as it has been observed that not only the trailing edge, but the laminar-turbulent transition region are efficient noise sources [9], [10]. The trailing-edge noise contributes at all frequencies, whereas transition/reattachment region at the leading edge has an effect on the high frequencies. Mainly, the broadband noise generation in the vicinity of the trailing edge is addressed in this work.

The investigation is carried out on the Controlled Diffusion (CD) airfoil [11], [12]. It is a cambered airfoil operated in industrial applications such as turbo-engine compressor and fan blades, and automotive engine cooling fans. In this study, the airfoil is immersed in the flow at a geometric angle of attack of 8°, a Reynolds number of 1.5×10^5 and a Mach number of 0.25.

The validation of the numerical results is made by means of experimental results. To do so, the simulations must include equivalent conditions [3]. The installation effects found in open-jet anechoic wind tunnels are included by immersing the airfoil in the potential core of the jet. The flow around the airfoil becomes non-uniform, the airfoil loading, boundary layer development, and flow separation are modified [13], which leads to a sound field modification.

II. Numerical modeling

A 3D DNS of the flow over the CD airfoil of chord c = 0.1356 m embedded in the jet potential core of a free-jet wind

EUR-TSAE,NSERC

tunnel at a chord-based Reynolds number of $Re_c = 1.5 \times 10^5$, free-stream Mach number $M = 0.25$, geometric angle of attack of 8°, and reference velocity $U_\infty = 16$ m/s is conducted.

A. *Flow field model*

The flow is governed by the non-dimensional full compressible Navier–Stokes equations. They are the conservation of mass (1), momentum (2) and energy (3). The normalization parameters are the airfoil chord, free-stream velocity, density and temperature. Finally, the non-dimensional state equation (4) with $\gamma = 1.4$ permits to close the system of equations, yielding:

$$\frac{\partial \rho}{\partial t} + \frac{\partial}{\partial x_j}\left(\rho u_j\right) = 0 \tag{1}$$

$$\frac{\partial}{\partial t}\left(\rho u_i\right) + \frac{\partial}{\partial x_j}\left[\rho u_i u_j + p\delta_{ij} - \tau_{ij}\right] = 0 \tag{2}$$

$$\frac{\partial}{\partial t}(\rho e) + \frac{\partial}{\partial x_j}\left[\rho u_j\left(e + \frac{p}{\rho}\right) + q_j - u_k \tau_{kj}\right] = 0 \tag{3}$$

$$p = \frac{\rho T}{\gamma M^2} \tag{4}$$

where the parameters e, τ_{ij} and q_i are the energy, molecular stress tensor and heat flux vector respectively.

The numerical code that is employed to perform the simulations is *HiPSTAR* (High Performance Solver for Turbulence and Aeroacoustic Research) [13]. It uses a 4$^{\text{th}}$-order central standard difference accurate scheme with Carpenter boundary stencils in the x-y plane and spectral approach in the spanwise direction. The 4$^{\text{th}}$-order accurate temporal discretization uses an ultra low-storage five-stage Runge-Kutta integration scheme.

The CD airfoil computations have been carried out on a reduced rectangular domain, as seen in Fig. 1. It permits to embed the airfoil in the core of the jet (see Fig. 2). The domain is centered at the trailing edge and it is extended 2 chords upstream, 2.5 chords downstream and 1 and 1.5 chords at the bottom and top boundaries respectively. The structured mesh is composed of two overlapping blocks: a background mesh (Block 1) and a superimposed O-grid around the airfoil (Block 2). The O-grid permits to obtain a high-quality refinement near the airfoil, allowing resolution of the laminar and turbulent boundary layers around the airfoil.

Following previous studies [14], the O-grid mesh is composed of 1000×140 grid points in the tangential and normal directions from the airfoil surface and 96 spanwise spectral modes covering the spanwise length of $0.1c$. This spanwise extent was proven to be sufficiently large [15].

The computation stability is ensured by setting a non-dimensional time step to 1.5×10^{-5}, which corresponds to a physical time step of 1.27×10^{-7} s. This time step provides a CFL < 1 in the domain. Finally, in the wall-normal direction, $y^+ < 1$ over most of the airfoil surface, with its maximum value $y^+_{\max} \approx 1.5$ at the leading edge.

The boundary conditions are such that they reproduce the experimental conditions of four different open-jet facilities with a jet width of 50 cm: Ecole Central de Lyon (ECL), Université de Sherbrooke (UdeS), Michigan State University (MSU) and the Technology University of Delft (TU-Delft).

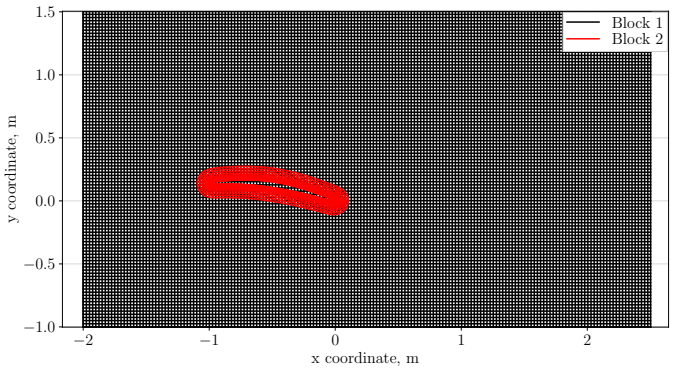

Figure. 1: Slice of complete domain meshing. Two-block structured mesh fitting the core of the jet. Every 10 gridlines of mesh shown.

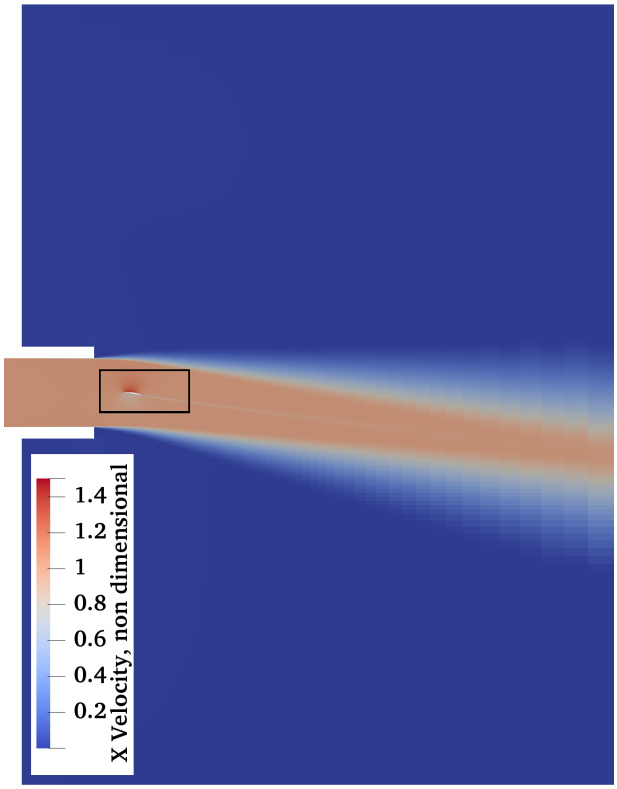

Figure. 2: Velocity contours of 2D RANS calculation employed as initialization and boundary values in the DNS. Black box showing the DNS domain limits.

Therefore, the installation effects that affect the airfoil loading are accounted for [8]. To do so, a 2D Reynolds-Averaged Navier-Stokes (RANS) simulation of the flow around the CD airfoil is first computed and used to introduce the initial mean flow field and boundary conditions in the DNS. Since the computational cost of the RANS calculation is much lower, the complete experimental geometric configuration is introduced in the domain. The turbulence model that is employed is the $k-\omega$ SST, which is meant to provide a good global behavior in this application [12]. The RANS velocity profiles found at the inlet and top boundary locations in the DNS domain are used as inflow boundary conditions.

B. Acoustic field model

The acoustic radiation from the CD airfoil is investigated by coupling the DNS results with the in-house Ffowcs-Williams & Hawkings (FWH) solver *SherFWH*. In the solid formulation used here, the far-field acoustic pressure is computed from the wall-pressure fluctuations over the CD airfoil. Two main terms compose the far-field acoustic pressure: monopolar (thickness noise), and dipolar (loading noise).

$$p'(\mathbf{x},t) = \frac{\partial}{\partial t}\int_{f=0}\left[\frac{Q_i n_i}{4\pi|\mathbf{x}-\mathbf{y}|}\right]_{\tau_e} \mathrm{d}S + \\ -\frac{\partial}{\partial x_i}\int_{f=0}\left[\frac{L_{ij} n_j}{4\pi|\mathbf{x}-\mathbf{y}|}\right]_{\tau_e} \mathrm{d}S \tag{5}$$

The airfoil surface becomes the control surface which encloses the noise sources to be accounted. The sampling frequency of the wall-pressure fluctuations is taken at about 78 kHz.

III. Results

In this section, the results for the CD airfoil under installed conditions are shown. Both aerodynamic and aeroacoustic fields are evaluated. The flow passing over a CD airfoil deals with several complex physical processes on the suction side: leading edge laminar separation, laminar-turbulent transition which leads to flow reattachment and finally, flow leaving the airfoil at the trailing edge producing a small trailing-edge vortex shedding. In Fig. 3, these effects are shown. The leading edge laminar separation turns into a Laminar Separation Bubble (LSB) close to the leading edge, on the initial 10% of the chord.

The time and spanwise averaged wall-pressure coefficient defined in (6) is shown in Fig. 5. The reference free-stream pressure p_∞, density ρ_∞ and velocity U_∞ are used to normalize the time- and spanwise-averaged wall-pressure distribution $\langle p \rangle$.

$$C_p = \frac{\langle p \rangle - p_\infty}{\frac{1}{2}\rho_\infty U_\infty^2} \tag{6}$$

This effect is consistent with the DNS studies of Wu [8], but the LSB is slightly larger than in the experimental campaigns at ECL, UdeS and TU-Delft and the 2D RANS simulation. The turbulence intensities in these wind tunnels were about 0.8%, 0.4% and 0.2% respectively, whereas in the DNS, no inlet turbulence is introduced. The pressure coefficient shows

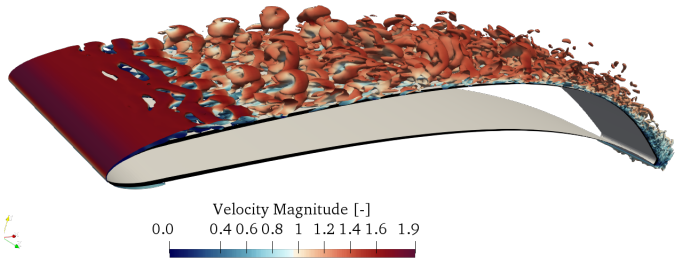

Figure. 3: Instantaneous field of Q-criterion, velocity magnitude. Leading-edge detail, DNS results.

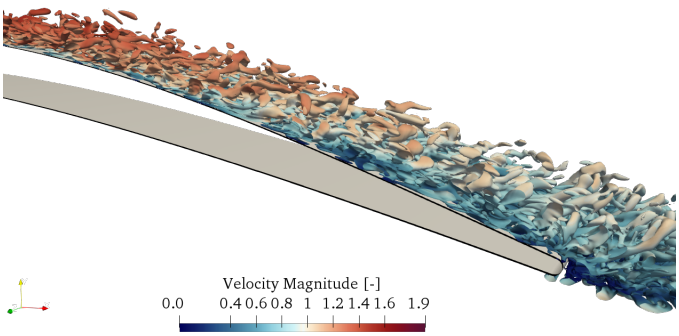

Figure. 4: Instantaneous field of Q-criterion, velocity magnitude. Trailing-edge detail, DNS results.

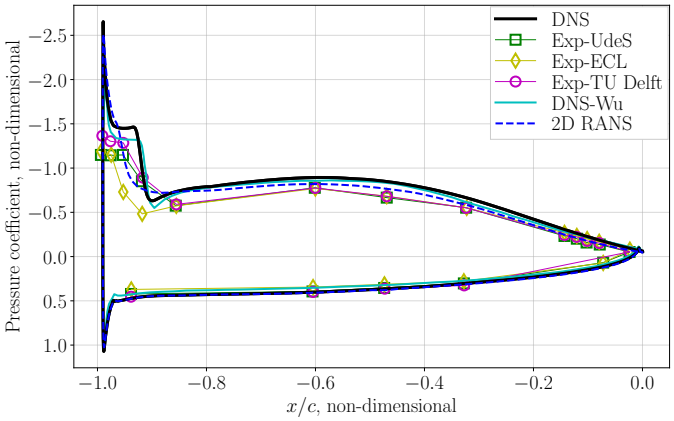

Figure. 5: Temporal and spanwise mean value of the pressure coefficient C_p

that the installation effects have been properly reproduced in the DNS setup. The RANS turbulence model provides a good approximation to the experimental LSB size.

The mean (Fig. 6) and fluctuating (Fig. 7) velocity profiles in the near wake are evaluated as well to check the validity of the DNS flow computations. Again, numerical and experimental data of the CD airfoil are employed to compare the results. The experimental data comes from Hot Wire (HW) and Particle Image Velocimetry (PIV) experimental campaigns from MSU and UdeS respectively. Details on the boundary layer profiles can be found in [14]. In addition, four wake positions located farther downstream are evaluated in Fig. 8 and compared to the analogous RANS velocity profiles.

The horizontal component of the mean velocity, u, shows a good agreement with the available data. In general, the best match is found between the PIV data and the numerical data. At the closest point to the trailing edge, the velocity drop found in the present DNS is slightly lower than expected. Notice that the RANS profiles show in all cases, a smoother evolution towards the wake velocity deficit peak.

At the closest point to the trailing edge, the vertical component of the mean velocity, v, produces a shift in this velocity component outside the wake region, as seen in Fig. 6c. There is about 20% discrepancy in its asymptotic value. It may imply a slight modification on the airfoil loading. However, when moving farther from the trailing edge, the vertical velocity

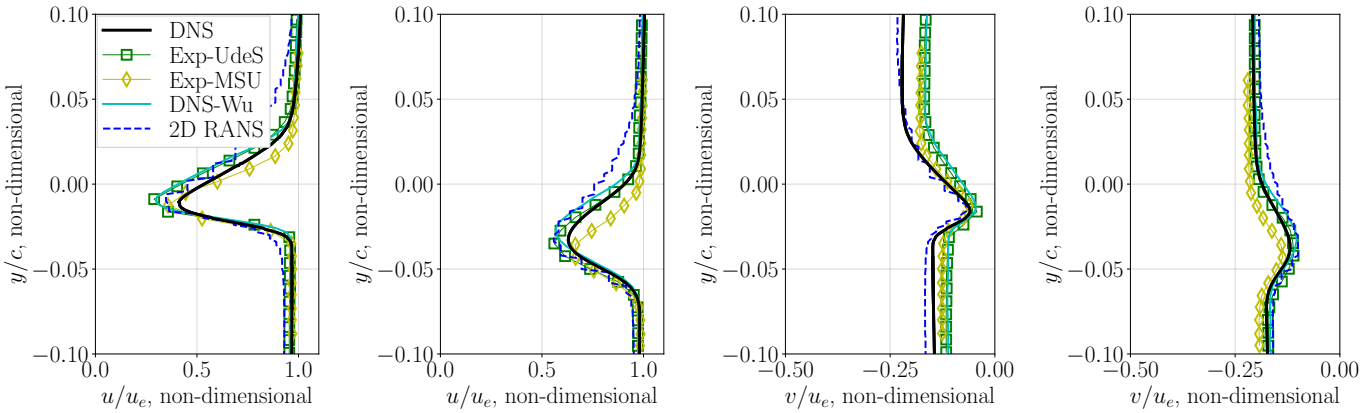

(a) Horizontal velocity component at $x/c = 0.075$.
(b) Horizontal velocity component at $x/c = 0.206$.
(c) Vertical velocity component at $x/c = 0.075$.
(d) Vertical velocity component at $x/c = 0.206$.

Figure. 6: Near wake velocity profiles. Vertical cuts at two positions from the airfoil trailing edge, separating horizontal and vertical velocity components. DNS compared to 2D RANS case, experimental, and DNS data extracted from Wu *et al.* [8].

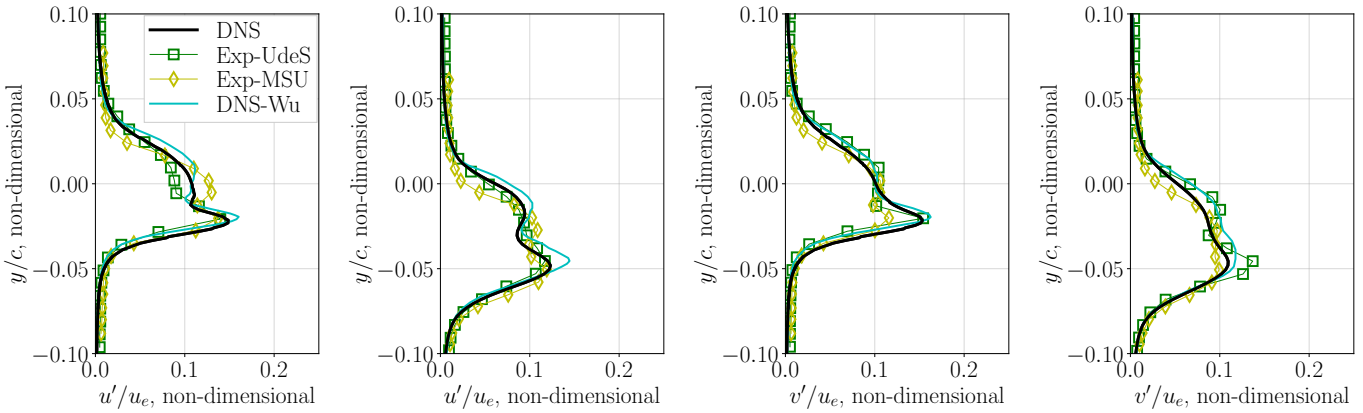

(a) Horizontal velocity component at $x/c = 0.075$.
(b) Horizontal velocity component at $x/c = 0.206$.
(c) Vertical velocity component at $x/c = 0.075$.
(d) Vertical velocity component at $x/c = 0.206$.

Figure. 7: Near wake fluctuating velocity profiles. Vertical cuts at two positions from the airfoil trailing edge, separating horizontal and vertical velocity components. DNS compared to 2D RANS case, experimental, and DNS data extracted from Wu *et al.* [8].

component of the flow unaffected by the wake follows the marked trends from the experimental and numerical available data. Furthermore, the effects in the wake do not show any modifications in the peak velocities. Thus, it can be assumed that the aforementioned discrepancy might be due to the RANS uncertainty on the velocity profiles imposed at the boundaries.

The fluctuating velocity profiles show a good overall agreement as well. However, there is some peak amplitude reduction in the wake deficit, most noticeable in Fig. 7d. This damping might be due to undesired dissipation introduced by the spatial interpolation as there is a discontinuity in between cell sizes from the O-grid and cartesian overset mesh. With that, it is seen that the computed DNS provides a reliable hydrodynamic field, which is required to evaluate the acoustics.

The farther from the airfoil, the velocity profile shows a damping in amplitude of the velocity deficit as well as a shift of the position of the deficit peak. It corresponds to the progressive dissipation of the wake as it approaches to the outlet and its alignment with the inflow direction.

The noise spectrum at a distance of 2 m from the trailing edge, at 90° is shown in Fig. 9. The noise predicted with *SherFWH* is presented together with previous experimental and numerical results. There is a general good agreement with experiments carried out at ECL as well as UdeS from low to medium frequencies. Nonetheless, in the present study, at high frequencies, there is a drop in the sound pressure levels.

The dilatation field (Fig. 11) can illustrate the acoustic field. Two methods can be employed to yield the dilation field from the continuity equation: either the velocity divergence or the temporal derivative of density. The temporal derivative of the density is less sensitive to computational errors, since it is not dependent on the spatial gradients. The dilatation contours of the flow field computed by means of the temporal derivative of density are shown in Figs. 10 and 11.

$$-\frac{\partial \rho}{\partial t} = \rho \left(\nabla \cdot \mathbf{u} \right) \tag{7}$$

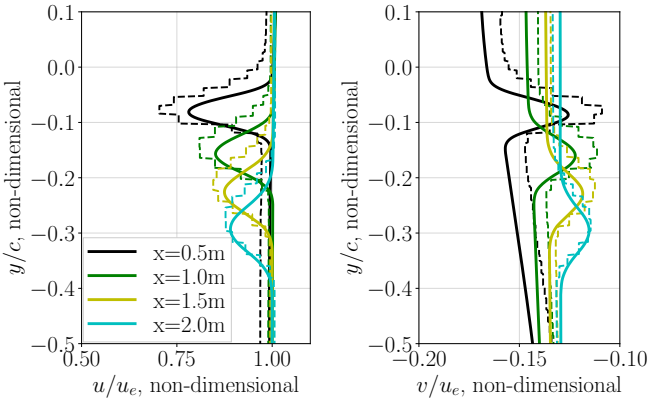

(a) Horizontal velocity. (b) Vertical velocity.

Figure. 8: Farther wake velocity profiles. Vertical cuts at four positions from the airfoil trailing edge, separating horizontal and vertical velocity components. DNS (dashed lines) compared to RANS (solid lines).

The instantaneous contours of the Q-criterion (second invariant of the velocity gradient tensor) colored by the velocity magnitude are shown in Fig. 11. The velocity contours show the flow evolution over the airfoil surface. On the suction side, the flow transitions from laminar to turbulent with the presence of the LSB close to the leading edge seen in Fig. 5. From mid-chord to the trailing edge, the flow remains attached on the suction side (on the verge of separation due to the high local adverse pressure gradient). On the pressure side, the flow transition to turbulence occurs near the trailing edge, yielding a small vortex shedding. The latter is evidenced in Fig. 11.

The dilatation contours show the noise sources close to the airfoil. They are mainly linked to the LSB, the flow detachment/reattachment over the airfoil surface and a third source downstream, near the trailing edge.

The dilatation field is pass-filtered for the low (Fig. 10a) and high frequencies (Fig. 10b). This filtering is performed with the aim of determining the frequency contribution of the

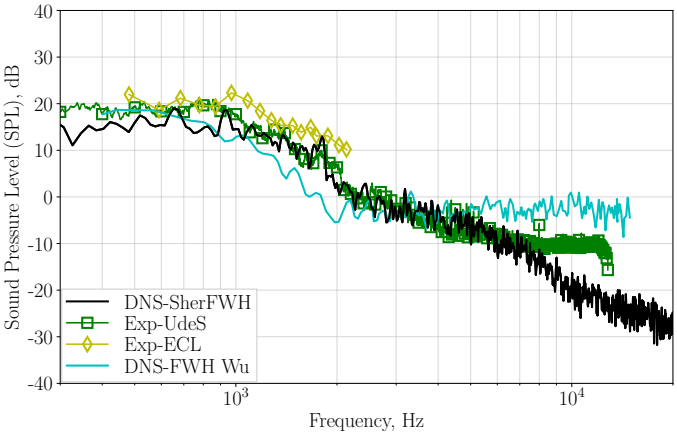

Figure. 9: Sound Pressure Levels at 2 m from the trailing edge, in the perpendicular direction to the suction side. Data compared to experimental and numerical data available.

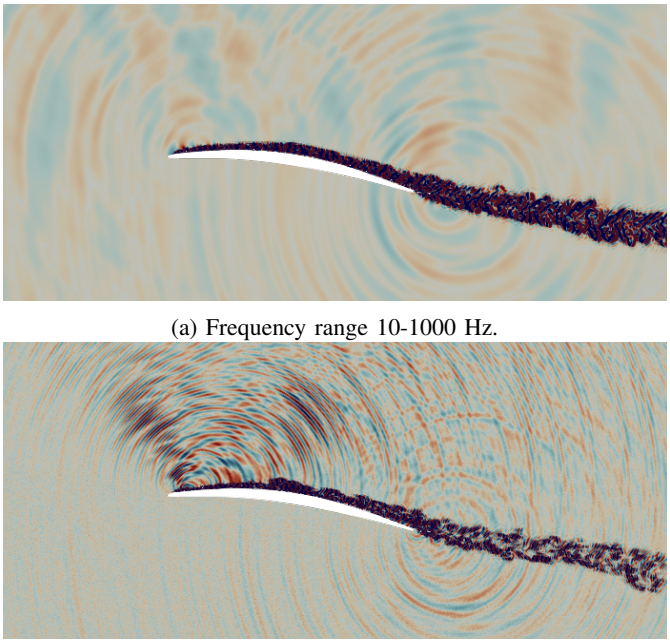

(a) Frequency range 10-1000 Hz.

(b) Frequency range 4-5 kHz.

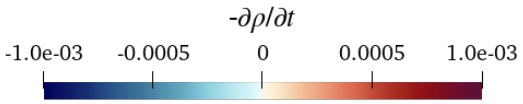

Figure. 10: Contours of filtered dilatation field ($-\partial\rho/\partial t$).

noise sources. To do so, the time derivative of the density field is Fourier Transformed to obtain its evolution in the frequency domain, then, they are filtered according to the frequency range to later perform an inverse Fourier Transform to achieve the filtered $\partial\rho/\partial t$. At low frequencies, noise is produced by the combination of the three noise sources aforementioned. When increasing the frequency, the source in the near wake starts to become as important as the noise source found in the LSB. Still, the noise due to the turbulent boundary layer and wake are the main noise sources of this study.

The solid formulation of the FWH analogy that is employed does not include the noise source in the near wake seen in Figs. 11 and 10b. This might be responsible for the drop at high frequencies that does not appear experimentally in the sound pressure levels.

IV. Conclusion

A compressible DNS of the flow over a Controlled Diffusion airfoil at a geometric angle of attack of 8°, a chord-based Reynolds number $Re_c = 1.5\times10^5$ and free-stream Mach number $M = 0.25$ has been carried out with the aim of studying the relationship between the near field and far field acoustics and how they relate to noise generation mechanisms. In order to validate the numerical results by means of experimental data, the installation effects are included in the simulations.

The aerodynamic results show compliance with the experimental campaigns of ECL, UdeS and MSU. The computed wall-pressure coefficient provides evidence of a laminar separation bubble slightly bigger than the one found in experiments, most likely because of the lack of turbulence inflow

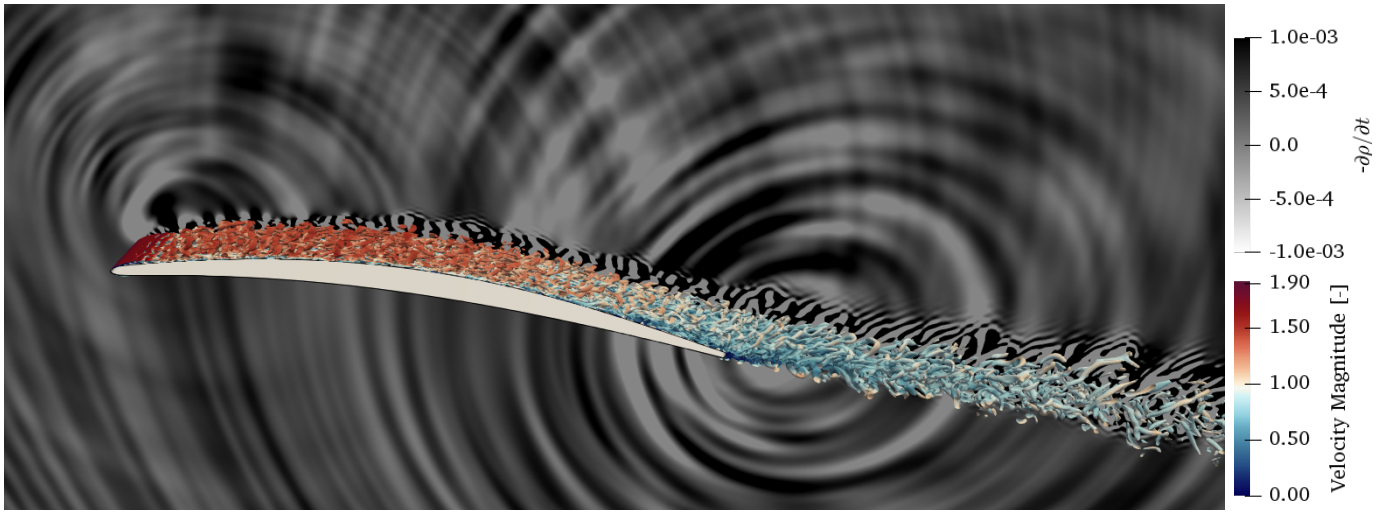

Figure. 11: Instantaneous field of Q-criterion velocity magnitude superimposed to the dilatation field contours ($-\partial\rho/\partial t$). DNS results.

specified in the simulations. The mean and fluctuating velocity profiles found in the near wake show good agreement with the experimental wake deficit.

The far field noise is predicted by using the solid approach of the FWH formulation and at low to mid frequencies the predicted sound pressure levels at a distance of 2 m from the trailing edge correspond to the ones found experimentally. The noise sources are evaluated and three main noise sources appear:

1) The flow separation and reattachment at the leading edge on the suction side, which produces a laminar separation bubble.
2) Interaction between the attached turbulent flow over most of the airfoil suction side.
3) A noise source in the near wake, close to the trailing edge.

The effect of the two first noise sources appears all over the frequency content, whereas the third source only contributes at higher frequencies.

Acknowledgment

This work was partly supported by the French "Programme d'Investissements d'avenir" EUR-TSAE. We also acknowledge the support of the Natural Sciences and Engineering Research Council of Canada (NSERC). This research was undertaken with the assistance of resources and services from the Digital Research Alliance of Canada and the National Computational Infrastructure (NCI), which is supported by the Australian Government.

References

[1] S. Lee, L. Ayton, F. Bertagnolio, S. Moreau, T. P. Chong, and P. Joseph, "Turbulent boundary layer trailing-edge noise: Theory, computation, experiment, and application," *Progress in Aerospace Sciences*, vol. 126, no. June, p. 100737, 2021.

[2] J. E. Ffowcs-Williams and L. H. Hall, "Aerodynamic sound generation by turbulent flow in the vicinity of a scattering half plane," *Journal of Fluid Mechanics*, vol. 40, no. 4, pp. 657–670, 1970.

[3] R. Boukharfane, M. Parsani, and J. Bodart, "Characterization of pressure fluctuations within a controlled-diffusion blade boundary layer using the equilibrium wall-modelled LES," *Scientific Reports*, vol. 10, pp. 1–19, March 2020.

[4] M. Deuse and R. D. Sandberg, "Different noise generation mechanisms of a controlled diffusion aerofoil and their dependence on Mach number," *Journal of Sound and Vibration*, vol. 476, p. 115317, March 2020.

[5] R. D. Sandberg, N. D. Sandham, and P. F. Joseph, "Direct numerical simulations of trailing-edge noise generated by boundary-layer instabilities," *Journal of Sound and Vibration*, vol. 304, pp. 677–690, March 2007.

[6] M. Sanjosé, S. Moreau, M.-S. Kim, and F. Pérot, "Direct self-noise simulation of the installed Controlled Diffusion airfoil," *American Institute of Aeronautics and Astronautics*, 2011. 2011 AIAA/CEAS Aeroacoustics Conference.

[7] J. Winkler., H. Wu, S. Moreau, T. Carolus, and R. Sandberg, "Trailing-edge broadband noise prediction of an airfoil with boundary-layer tripping," *Journal of Sound and Vibration*, vol. 482, pp. 115450:1–25, 2020.

[8] H. Wu, S. Moreau, and R. Sandberg, "On the noise generated by a controlled-diffusion aerofoil at $Re_c = 1.5 \times 10^5$," *Journal of Sound and Vibration*, vol. 506, pp. 116152: 1–20, 2020.

[9] R. D. Sandberg and N. D. Sandham, "Direct numerical simulation of turbulent flow past a trailing edge and the associated noise generation," *Journal of Fluid Mechanics*, vol. 596, p. 353–385, 2008.

[10] L. E. Jones, N. D. Sandham, and R. D. Sandberg, "Acoustic source identification for transitional airfoil flows using cross correlations," *American Institute of Aeronautics and Astronautics*, vol. 48, pp. 2299–2312, 2010.

[11] S. Moreau, M. Henner, G. Iaccarino, M. Wang, and M. Roger, "Analysis of Flow Conditions in Freejet Experiments for Studying Airfoil Self-Noise," *American Institute of Aeronautics and Astronautics*, vol. 41, pp. 1895–1905, October 2003.

[12] S. Moreau and M. Roger, "Effect of Airfoil Aerodynamic Loading on Trailing-Edge Noise Sources," *American Institute of Aeronautics and Astronautics*, vol. 43, pp. 41–52, January 2005.

[13] R. D. Sandberg, "Compressible-flow DNS with application to airfoil noise," *Flow Turbulence Combust*, vol. 95, pp. 211–229, May 2015.

[14] A. Arroyo Ramo, S. Moreau, R. D. Sandberg, M. Bauerheim, and M. C. Jacob, "Direct Numerical Simulation of Controlled Diffusion airfoil," *28th AIAA/CEAS Aeroacoustics Conference*, pp. 1–22, jun 2022.

[15] M. Wang and P. Moin, "Computation of trailing-edge flow and noise using large-eddy simulation," *American Institute of Aeronautics and Astronautics*, vol. 38, pp. 2201–2209, January 2000.